3D defect detection using weighted principal component thermography

3D Defect detection using weighted principal component thermography

Seppe Sels , Boris Bogaerts, Simon Verspeek, Bart Ribbens, Gunther Steenackers, Rudi Penne, Steve Vanlanduit

Op3Mech, University of Antwerp, Groenenborgerlaan 171 , 2020 Antwerp Belgium

Abstract

Quantitive infrared thermography like active thermography is a non-destructive testing technique that is used to inspect surfaces of components for defects. A problem with infrared-based defect detection is that misclassifications based on geometrically dependent measurement characteristics can occur. This problem becomes more problematic with the inspection of complex 3D shapes. In this paper, a new infrared quality control procedure using a quality map is proposed that models the geometrically dependent measurement characteristics based on available CAD data and CAD matching techniques. Misclassifications are reduced by using this quality map in combination with a modified version of principal component thermography post-processing. We applied our proposed methodology on a prototype bicycle part and a plaster cast angel figurine. In these experiments, the procedure using quality maps is able to prevent false defect detection.

Keywords: Thermography, 3D, Matching, Active Thermography, Pulsed Thermography, Principal Component Analysis, Principal Component Thermography, 3D Thermography, Infrared Imaging

1. Introduction

Quantitative infrared thermography such as active thermography is a non-destructive testing technique that is used to rapidly inspect the surface and subsurface of a component for defects. In scientific literature, usually, measurements on simple components (like flat panels) are presented. The use of measurements on complex 3D shapes is more complicated because it is difficult to quantify the defect size, 3D location and corresponding material properties using the 2D information represented in the infrared image [1]. However, when the 3D locations of the measured temperatures are obtained, this size and location of the defects can be measured [2]. Secondly, the 3D location can be used to visualise and combine several measurements from different viewing angles. Finally, when the direction with respect to the camera of a measured object is available, the influence of directional emissivity can be characterised and compared with numerical simulations based on CAD data [3].

In literature, different approaches that map 2D infrared images to 3D locations exist. Commonly, these methods obtain location information by using additional 3D range camera's, structured light scanners or laser scanners to map 2D infrared images to a 3D position [4, 5, 6, 7, 8, 9]. Methods that do not use additional equipment but only a 3D model of the test object also exist [10, 11, 12, 13]. In this work, an implementation of the method of Prisacariu et al. [12] is used.In summary, the algorithm calculates the possibility if a pixel contains foreground or background information. After this, a virtual image of a 3D model is taken and compared with these possibilities. Next, the pose of the virtual camera will be updated so that the fore- and background regions of the real image and the virtual image align. Although the alignment accuracy is object and camera dependant, an accuracy of approximately 5 pixels can be easily achieved [14, 15]. Alternative systems use accurate position control of a component using traverse systems or robots to position a detected defect on the component [16] accurately.

This work describes a methodology which improves the use of 3D infrared mapping techniques. The proposed methodology uses quality maps of the 3D mapping and uses image segmentation techniques in combination with a weighted version of principal component thermography [17, 18] to automatically detect defects and material types on objects. To our knowledge, a weighted version of principal component thermography (PCT) is not used in current implementations. In the PCT algorithm, a principal component analysis (PCA) is used. In this part, we will introduce weights since for PCA various weighted algorithms exist.

This paper focuses on the analysis of measurement data obtained with 3D thermography. This analysis in the form of what we call 'quality maps' is described in Section 2. To illustrate the procedure in Section 2 a 3D printed model of the Stanford Bunny (Stanford Computer Graphics Laboratory [19]) is used in example images. The procedure to calculate defects of a surface

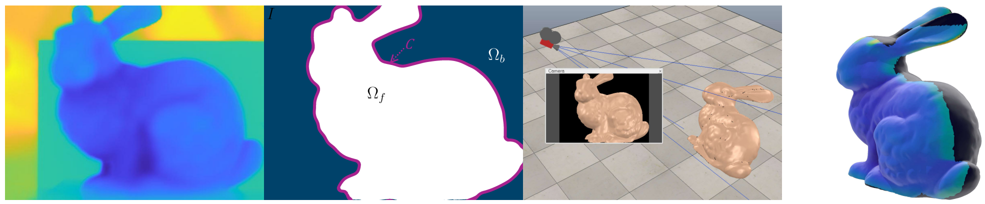

(a) (b) (c) (d)

Figure 1: (a) Example infrared image of a Stanford bunny (colours for visualisation) (b) Contour image rendered with the virtual scene (c) Example of a scene with a virtual camera and 3D model of the bunny. (d) Result of the image alignment where the thermal information from (a) are plotted on the 3D model. Black parts of the model are parts where no data is available. Small shadow effects are added to the render for better visualisation.

using 3D data is described in Section 3. The experimental setup and experimental results displayed on a restored plaster angel figurine and a prototype of a bicycle frame together with an automatic calculation of the defects are given in Sections 4 and 5.

2. Methodology: quality of mapping

Principal component thermography is a technique used in active thermography to analyse the heat response of a test object using principal component analysis (PCA). This analysis highlights differences in material properties in the image by constructing temporal modes [17, 20]. Temporal modes are images constructed with a corresponding principal component calculated from a singular value decomposition of a time series of infrared images. With active thermography, this time series is the recording of the heat-up or cool-down characteristics of an object. Ideally, when the analysed material is uniform, the first mode highlights the primary material. Next, the second mode will highlight the most significant defects or a secondary material. Work of Marinetti et al. [17] shows that 95% of the main differences in material properties on flat surfaces are detectable in the first 3 to 5 modes.

In reality, this analysis is distorted by multiple environmental factors:

- factor 1 The image contains background information. This information is not part of the test object but is used in the principal component thermography calculations.
- factor 2 The normal of the surface is not perpendicular to the camera sensor [16]. This introduces an error in the measured emissivity recorded

by the camera. These errors can result in false-positive fault detections because these areas will correspond with different principal components in the principal component thermography analysis.

factor 3 The spatial resolution of the thermal camera is too low to detect a small change in material properties, e.g. a defect is smaller than 1 pixel in the camera image.

factor 4 The distance between the object and the camera increases the noise in the recordings (emissivity of the atmosphere) and/or can give problems when focusing the lens. In our setup transmissivity is neglected because it only influences results when objects are located more than 3 meter [21].

This work aims to solve these problems by using the known pose of the test object and the corresponding 3D model. In the next paragraphs, we will explain how virtual views of the object are used to segment foreground and background. Moreover, we will also show how to calculate a quality map of the measurement that quantifies the described environmental factors. This quality map Q is used in the singular value decomposition to compensate for low-quality measurements. Pixels with $Q = 1$ are pixels with a high quality where no error in the measurement is expected. Pixels with $Q < 1$ are pixels where measurements errors might occur. Next, the quality-map is used in combination with a weighted version of principal component thermography to detect differences in material properties of the surface of an object (Section 3).

The quality map Q is composed of three parameters (see next Sections) that quantify the mentioned environmental parameters:

1. Normalised distance G_n between a pixel p and the contour of the object C (factor 1).
2. Normalised spatial distance S_n: Each measured point has a corresponding 3D coordinate from the CAD matching procedure. With this correspondence, the distance between measured points (pixels) can be calculated (factor 2 and 3).
3. Depth D_f of a measured point (factor 4).

Only three parameters describe the four environmental parameters because the normalised spatial distance describes both factor 2 and factor 3 (see next Section). As a total weight that can be used as a quality measurement Q we propose:

$$Q = G_n D_f S_n \tag{1}$$

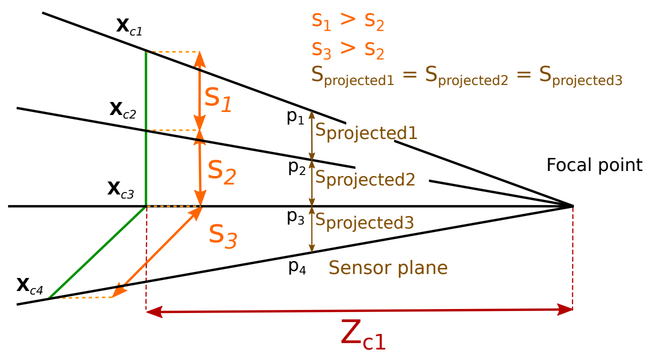

Figure 2: Example of differences in spatial distances s_i and their constant projections $s_{\text{projected}}$. X_c represents a 3D point of the object detected by the camera sensor.

giving values between 0 and 1.

2.1. Notation

An image (Figure 1a) is denoted as I with the image domain $\Omega \subset \mathbb{R}^2$, Ω_f is the foreground image domain and Ω_b is the background image domain. An image pixel is denoted as $p = [u, v]$ with $I(p)$ a grey scale value (related to thermal information in infrared images). A pixel coordinate $p \in \Omega_f$ has a corresponding 3D point in the camera coordinate system $\mathbf{X_c} = [X_c, Y_c, Z_c]^T \in \mathbb{R}^3$. This 3D point is obtained from a CAD matching procedure using a 3D model of the object or a calibrated range camera setup (see Section 1).

C (Figure 1b) is the projected contour of the 3D model (Figure 1c) in the camera image. This contour separates the foreground and background domains Ω_f, Ω_b.

2.2. Quality maps

The depth of a pixel is also an important parameter because all cameras have a depth-of-field where the camera is in focus. In this work we define depth of field D_f as:

$$D(p_i) = \frac{1}{\sigma\sqrt{2\pi}} e^{-\left(Z_c(p_i)-d_{focal}\right)^2 / 2\sigma^2} \tag{2}$$

which gives values of the normal distribution with $Z_c(p_i)$ (see Figure 2) the depth of a pixel p_i from the camera reference frame. d_{focal} is the distance from the camera where an object is in focus and σ the standard deviation describing the Gaussian blur occurring when an object is out of focus. An example is given in Figure 3b. In this example and in our experiments we assumed $d_{focal} = min(Z_c)$ (the closest point to the camera) and $\sigma = 2\,\text{cm}$. This is done because the camera is manually focused at the front of the object and experimentally we found that a standard deviation of $\sigma = 2\,\text{cm}$ resembles the blur in the image.

Due to the perspective nature of a camera lens, the spatial distance between pixels will be larger near the edges of the image and smaller in the center of the image, this is visible in Figure 2. Therefore, we use the spatial distance matrix S as an error measure. The spatial distance S also encodes the perpendicularity of the surface normal to the camera sensor. If a point is located far away from its nearest neighbour, this will give a higher value of S and means the point is part of a surface seen under an angle (Figure 2). An example of this spatial distance matrix S is visible in Figure 3a. Each element of $\mathbf{X_c}$ gives a 3D location to a pixel p_i. This can be calculated by projecting the 3D model under a detected pose (see Section 2.1) in a virtual camera model. Then the spatial distance S matrix consists of the set of points s_i. s_i is for each point the distance to its closest neighbour.

An example is given in Figure 3a. The distance between points can be used as a direct quality measure (in meter). Note that with this formulation, a low spatial distance means points are close to each other, resulting in higher quality measurements. The normalised spatial distance matrix S_n is defined as $S_n = \frac{S}{max(S)}$, ensuring values between 0 and 1.

For 3D thermal measurements, the distance between a contour and a pixel is also significant because when this distance is low, the pixel is most probably near the contour, where a small error in image alignment can cause a pixel of the background to be rendered on the 3D model. We define this distance function G as:

$$\phi(p_i) = \begin{cases} d(p_i, C) & \forall\ p \in \Omega_f \\ 0 & \text{otherwise} \end{cases} \tag{3}$$

$$G(p_i) = H_e(\phi) \tag{4}$$

Where $d(p_i, C)$ is the smallest distance (in pixel) between the contour C and the corresponding pixel. The use of the smoothed Heaviside function $H_e(\phi) = \pi^{-1}(-\arctan(b\phi) + (\pi/2))$ allows to only give large weights to pixels near the edges of the contour. In all our experiments b is set to 3. This value is found experimentally, and worked well in all our test cases. The normalised

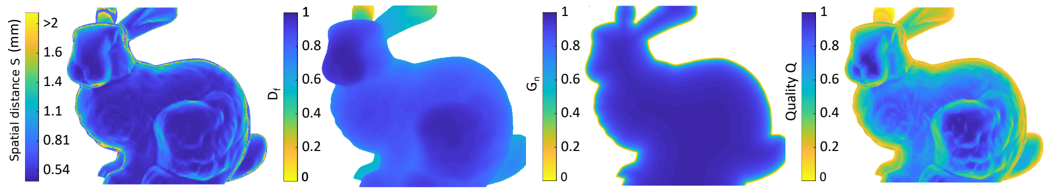

(a) (b) (c) (d)

Figure 3: In all images blue refers to higher quality points and yellow to a lower quality. (a) Example of the spatial distance. (b) The normalised distance to the contour. (c) Depth of field quality. (d) Combined quality of mapping.

distance G_n is defined as $G_n = G$, since the smoothed Heaviside function already ensures values between 0 and 1. An example is given in Figure 3c.

2.3. Quality of mapping

The three quality measurements (S_n,D_f,G_n) can be used independently if needed. As an example, the normalised spatial distance S_n can be used as an indication of the error on the length of a measured defect. As a total weight that can be used as a complete quality map Q we propose the product of the normalised quality measurements (see Equation 1). This product will ensure Q consists of values between 0 and 1.

In Figure 3, a pose of the model of the Stanford bunny is used as an example where the three quality maps are calculated and combined. This figure shows that, as expected, the quality near the edges of the object is low. The quality is also low at the transition of neck to head and at the upper side of the leg. The highest quality is located in the leg of the model. In this part, the camera is focused, the mapping is accurate, the spatial resolution is the highest, and the surface is parallel to the camera sensor. Quantifying this quality directly from the thermal image without using additional information of the 3D model and position of the object is not possible.

The quality map can also be used as a weighting factor to combine overlapping measurements on a 3D model. This is useful in cases where multiple images are taken to compose a complete thermal image of an object. Composing images can, for example, be used in engineering cases to visualise the energy efficiency of buildings [22].

3. Methodology: defect detection

When executing active thermography measurements, the test sample is heated for a defined time period. In our experimental setup (see Section 4) the heat response (cool-down) is recorded. From this entire image time-sequence, a principal component analysis (PCA) is performed. The standard algorithm used in thermography (PCT: principal component thermography) is available in the work of Marinetti et al. [17]. Differences with our proposed procedure are summarised in Algorithm 1. In the first step of the PCT algorithm, the image sequence (Data) is converted to a 2D matrix (WarpedData). In a standard PCT analysis, background pixels are not removed from this matrix. With our methodology, this is possible. Next, the matrix is normalised (NormData), and a singular value decomposition is performed. In the proposed algorithm, this singular value decomposition uses weights Q. Next, the TemporalModes are calculated, and the dimensions of this matrix are warped so that the first two dimensions contain image data, and the third includes the mode.

Algorithm 1 Weighted Principal Component Thermography

Input: Heat response: Time sequence of images ; Q
Output: Thermal Modes

1: WarpedData = Warpdata(Data) ▷ Make 2D matrix from 3D matrix (time in second dimension)
2: WarpedData = RemoveBackgroundPixels(WarpedData) ▷ Not done in standard PCT
3: NormData = (WarpedData-mean(WarpedData)) / std(WarpedData)
4: Calculate USV = BIRSVD(NormData,Q) ▷ No weights in standard PCT
5: TemporalModes = U S
6: TemporalModes= DeWarpData(TemporalModes) ▷ dim 1-2=image data ; dim 3=mode
7: Analyse TemporalModes

In this work, the standard SVD algorithm is replaced by a Bi-Iterative Regularized Singular Value Decomposition (BIRSVD) developed by Dasa et al. [23]. This implementation of the SVD algorithm additionally allows the use of weights in the calculations to compensate for low quality or missing data. Other algorithms and implementations exist and are described in literature[24, 25, 26, 27]. In this work the BIRSVD algorithm is used because of its relatively easy implementation reported performance. We also removed the background ($Q = 0$) from the input data, to eliminate the background values from the normalisation step and SVD calculation. The altered algorithm is summarised in Algorithm 1. The removal of the background ensures that the primary material of a test object is highlighted in the first temporal mode calculated by the algorithm. The use of the quality map ensures that the second mode corresponds with the secondary material or most substantial defects. This is not true in the original algorithm because edges and other factors (see Section 2) can distort the results and spread these properties over multiple modes [17]. Examples can be found in Section 5.

4. Experimental setup

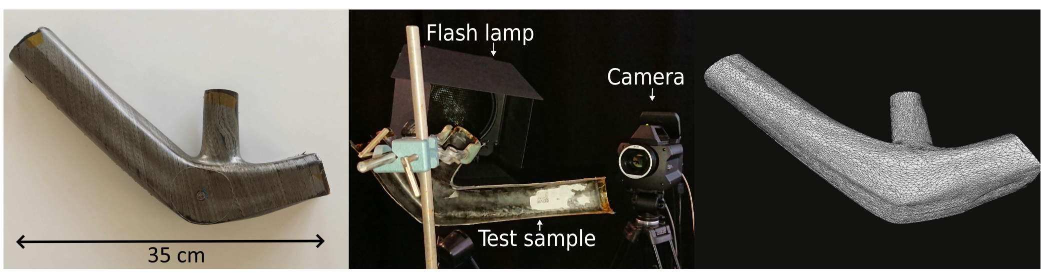

(a) (b) (c)

Figure 4: Experimental setup. (a) Image of bicycle test sample. (b) Clamped bicycle part with camera FLIR X6540sc and flash light.(c) Used 3D model (3D scanned mesh file)

In this work, active (pulsed) thermography is used in the validation of the procedure proposed in Section 2. As a first test sample, a plaster cast figurine of an angel is analysed. The figurine is heated with a halogen lamp (500 W) for 60 s. Next, the heat response (cool-down) is recorded (2000 frames, 50 fps) using a cooled infrared camera (FLIR X6540sc). In a second experiment, a prototype part of a bicycle (Figure 4a) with its corresponding CAD file (Figure 4c) is used. In this experiment, a short heat pulse (1 ms) of 6 kJ is induced in the test sample using a Xenon flash lamp (Figure 4b). Next, the heat response of the sample is recorded with 2000 frames, at 50 fps with the cooled infrared camera. As a post-processing technique, the standard PCT analysis [17, 18] is compared with the proposed version using weights.

To be able to neglect reflections of surroundings, it is made sure that the surrounding objects of the experimental setup are at room temperature. As a CAD matching procedure, a pixel-wise posterior segmentation technique in combination with 3D pose optimisation (PWP3D) [10, 12, 28] is used for mapping 2D thermographic images on 3D models.

5. Experimental results

The detection methodology is tested on a cast figurine of an angel and a prototype bicycle part. The measurements of the bicycle part show that the quality map can be used to avoid to detect false defects.

5.1. Cast figurine

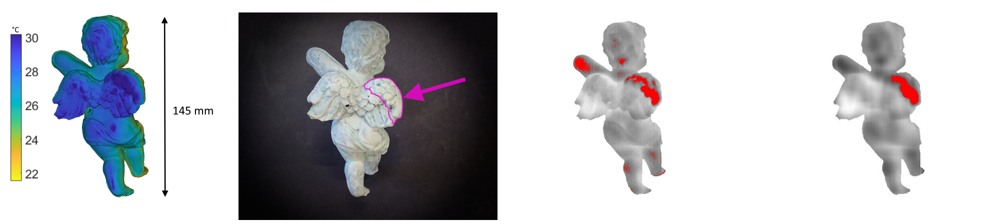

(a) 3D Infrared (b) Ground Truth (c) Standard PCA (d) Weighted PCA

Figure 5: (a) 3D infrared image (one image of the recording sequence) (b) RGB image with restored wing section (polymer modelling paste) in pink (c) Automatic determined defects/difference in material (red) with a standard PCA analysis (with the background removed). (d) Automatic determined defects/difference in material with the proposed weighted PCA. This weighted method does not include the false positives of the standard PCA method.

The proposed method is tested on a restored cast figurine of an angel. Initially, the figurine right wing was missing and is sculptured with polymer modelling clay. Next, the angel was repainted with acrylic paint to hide the restoration. The ground truth polymer clay restoration is highlighted in pink on the image in Figure 5b. The 3D shape is obtained by scanning the figuring with a structured light scanner (Faro Scan-In-A-Box).

The heat response of the figurine is recorded, and next the 3D pose is calculated. A mapped heat image on the 3D model is visible in Figure 5a. Afterwards, the quality map is calculated, and the heat response is analysed with the PCT analysis (with background removed) (Figure 5c) and the proposed PCT analysis using weights (Figure 5d).

The red parts are parts that correspond with a high chance of difference in material properties (highest 1 % values in the second temporal mode). In the standard PCT analysis (Figure 5c) parts of the head arm,legs and foot are highlighted incorrectly. The standard analysis also highlights surface edges. In this case, this is undesirable because these edges do not correspond with a change in material properties. In the image showing the weighted analysis using the quality map (Figure 5d) these edges are not highlighted. In contrast to the standard method, the proposed analysis highlights the wing correctly without false positives. The restored section has an area of 4705 pixels that is highlighted in the infrared image. The standard method highlights 3814 pixels, from which 2341 pixels are correctly highlighted (50 % of the restored area). The proposed method only highlights 2015 pixels of the true 4705 pixels (42 %), which is less than the standard method but has no false positives. The true positive pixel area is calculated by manually selecting the restored area in the 3D scan of the figurine.

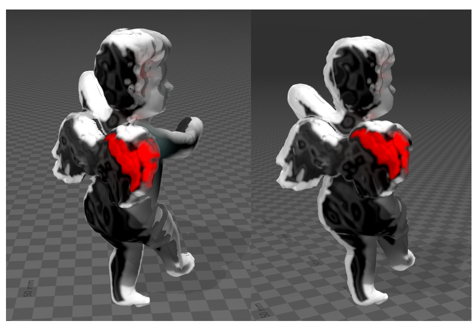

(a) (b)

Figure 6: 3D mapping of multiple (three) measurements. The red area corresponds with the detected restored areas using the same procedure as described on one image. White areas are areas that are not measured.

Figure 6 shows the mapping of multiple (three) measurements on the 3D model. The camera is positioned in three different positions and from each location, the weighted PCT method is used to calculate material differences. These differences are highlighted in red in the figure. In this case, weights of different measurements are not combined only the detected area from each analysis is highlighted. A combination of weights of different measurements can be investigated in future research.

5.2. Bicycle frame

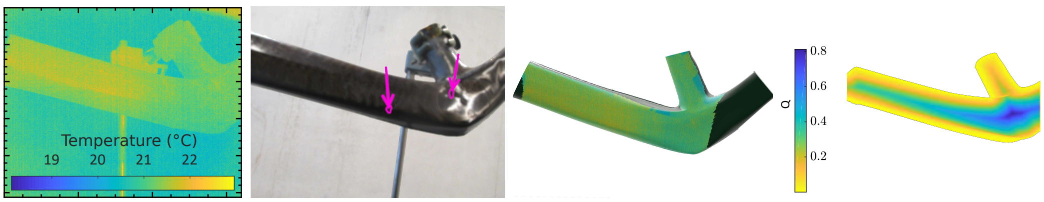

(a) (b) (c) (d)

Figure 7: (a) Reference image used in image alignment (b) defect locations (pink) (c) Aligned image mapped on 3D model (same temperature scale as (a), black parts have no data) (d) quality map of measurement

Figure 7a shows an infrared image of a prototype bicycle part. At two locations, the object is hit with an impact hammer (12 J). These locations are indicated in Figure 7b. The CAD mapping result is visible in Figure 7c and the quality map in Figure 7d.

From the complete heat response, the standard principal thermography analysis is performed. The third temporal mode is shown in Figure 8a. Figure 8b shows the segmented defects. Green areas are false positives detected with this method. These areas are also areas where the quality Q is below 0.5. Note that an additional image-open filter (image erosion followed by image dilation) is used to only highlight regions larger than 2 pixels.

In Figure 8c, the second temporal mode calculated with the weighted method is shown. Figure 8d shows the segmented defects in red. These defects correspond to the impacted locations.

6. Conclusion

Information on the alignment of an infrared image with a CAD file can be used to predict measurement artefacts in the form of a quality map. These predictions, together with a weighted version of the principal component thermography analysis, can be used to detect defects. In future research, the calculated position of the camera can also be used to cope with the directional behaviour of the emissivity when calculating temperatures out of the measured data. The use of the proposed methodology decreases the chance of false defects. The calculated quality map also gives the user a way to quantify possible measurement errors and optimise the setup by re-positioning the object and compare or combine results.

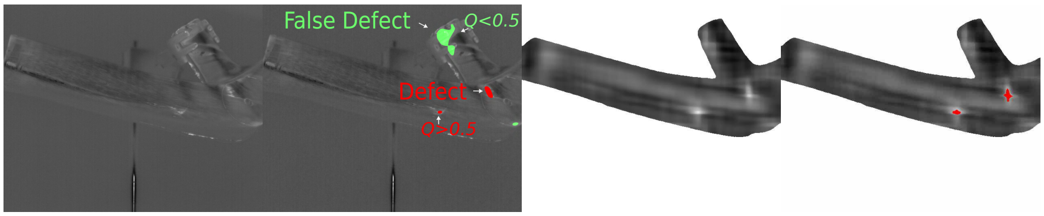

(a) Standard PCA (b) Standard PCA Segmented (c) Weighted PCA (d) Weighted PCA Segmented

Figure 8: (a) Temporal mode composed with standard PCA analysis. (b) Segmented defects where green denotes false defects and red positive defects (c) Temporal mode composed with weighted PCA analsyis (d) Segmented defects in red

Acknowledgements

Special thanks to Jeroen Peeters to assist the first measurements on the Stanford bunny and bicycle frame.

Special thanks to REIN4CED (https:/ /rein4ced.com) for providing the prototype bicycle component.

Funding

Research funded by:

Industrial Research Fund of the University of Antwerp (PS32388) ”3D imaging assisted vibration measurements for product testing and quality control”

Industrial Research Fund of the University of Antwerp (PSID-34924) ”Fast Broadband Lock-In Thermography for Fragile Structures Using System Identification”

TETRA fund of the Flanders Innovation & Entrepreneurship Agency (VLAIO) (HBC 0032 2017) ”Smart Integration of Numerical modelling with Thermal inspection, Sint”

Research Foundation-Flanders under grant Doctoral (PhD) grant strategic basic research (SB) 1S26216N (Boris Bogaerts) and 1SC0819N (Simon Verspeek).

Disclosures

“The authors declare that there are no conflicts of interest related to this article.”

7. References

[1] X. Maldague, Theory and Practice of Infrared Technology for Nondestructive Testing, Wiley, 2001.

[2] M. A. Akhloufi, Y. Guyon, C. I. Castanedo, A. Bendada, Three-dimensional thermography for non-destructive testing and evaluation, Quantitative InfraRed Thermography Journal 14 (2017) 79–106.

[3] J. Peeters, B. Ribbens, J. J. Dirckx, G. Steenackers, Determining directional emissivity: Numerical estimation and experimental validation by using infrared thermography, Infrared Physics and Technology 77 (2016) 344–350.

[4] B. Ribbens, J. Peeters, B. Bogaerts, G. Steenackers, S. Sels, R. Penne, G. V. Barel, 4D Active and passive thermography measurement system using a KUKA KR16 robot and time-of-flight imaging, 13th Quantitative Infrared Thermography Conference (2016).

[5] J. Rangel, S. Soldan, A. Kroll, 3D Thermal Imaging: Fusion of Thermography and Depth Cameras, in: Proceedings of the 2014 International Conference on Quantitative InfraRed Thermography, QIRT, 2014, pp. 35–40.

[6] Y. Cao, B. Xu, Z. Ye, J. Yang, Y. Cao, C.-L. Tisse, X. Li, Depth and thermal sensor fusion to enhance 3D thermographic reconstruction, Opt. Express 26 (2018) 8179–8193.

[7] P. Hellstein, M. Szwedo, 3D thermography in non-destructive testing of composite structures, Measurement Science and Technology 27 (2016).

[8] M. A. Akhloufi, B. Verney, Multimodal registration and fusion for 3D thermal imaging, Mathematical Problems in Engineering 2015 (2015) 1–14.

[9] S. Vidas, P. Moghadam, HeatWave: A handheld 3D thermography system for energy auditing, Energy and Buildings 66 (2013) 445–460.

[10] H. Tjaden, U. Schwanecke, E. Schömer, Real-time monocular segmentation and pose tracking of multiple objects, in: Lecture Notes in Computer Science (including subseries Lecture Notes in Artificial Intelligence and Lecture Notes in Bioinformatics), volume 9908 LNCS, pp. 423–438.

[11] K. Pauwels, D. Kragic, SimTrack: A simulation-based framework for scalable real-time object pose detection and tracking, in: IEEE International Conference on Intelligent Robots and Systems, volume 2015-Decem, pp. 1300–1307.

[12] V. A. Prisacariu, I. D. Reid, PWP3D: Real-time segmentation and tracking of 3D objects, International Journal of Computer Vision 98 (2012) 335–354.

[13] M. Corsini, M. Dellepiane, F. Ponchio, R. Scopigno, Image-to-Geometry Registration: a Mutual Information Method exploiting Illumination-related Geometric Properties, Computer Graphics Forum 28 (2009) 1755–1764.

[14] S. Sels, S. Verspeek, B. Ribbens, B. Bogaerts, S. Vanlanduit, R. Penne, G. Steenackers, A CAD matching method for 3D thermography of complex objects, Infrared Physics & Technology 99 (2019) 152–157.

[15] S. Sels, B. Bogaerts, S. Vanlanduit, R. Penne, Easy sensor localization using an RGB camera, in: ISMA 2018 ISBN 9789073802995, Katholieke Universiteit Leuven, 2018, pp. 1–6.

[16] J. Peeters, B. Ribbens, B. Bogaerts, S. Sels, J. Dirckx, G. Steenackers, V. U. Brussel, Optimized setup modification for automated active thermography, in: International Workshop on Advanced Infrared Technology and Applications, AITA 2017, pp. 121–124.

[17] S. Marinetti, E. Grinzato, P. G. Bison, E. Bozzi, M. Chimenti, G. Pieri, O. Salvetti, Statistical analysis of IR thermographic sequences by PCA, Infrared Physics and Technology 46 (2004) 85–91.

[18] E. D'Accardi, D. Palumbo, R. Tamborrino, U. Galietti, Quantitative analysis of thermographic data through different algorithms, Procedia Structural Integrity 8 (2018) 354–367.

[19] G. Turk, M. Levoy, Zippered polygon meshes from range images, in: Proceedings of the 21st annual conference on Computer graphics and interactive techniques - SIGGRAPH '94, ACM Press, New York, New York, USA, 1994, pp. 311–318.

[20] D. Griefahn, J. Wollnack, W. Hintze, Principal component analysis for fast and automated thermographic inspection of internal structures in sandwich parts, Journal of Sensors and Sensor Systems 3 (2014) 105–111.

[21] Q. H. Tran, D. Han, C. Kang, A. Haldar, J. Huh, Effects of ambient temperature and relative humidity on subsurface defect detection in concrete structures by active thermal imaging, Sensors (Switzerland) 17 (2017).

[22] S. Lagüela, J. Armesto, P. Arias, J. Herráez, Automation of thermographic 3D modelling through image fusion and image matching techniques, Automation in Construction 27 (2012) 24–31.

[23] S. Dasa, A. Neumaiera, Fast Regularized Low Rank Approximation of Weighted Data Sets, mat.univie.ac.at (2011) 1–29.

[24] I. Portnoy, K. Melendez, H. Pinzon, M. Sanjuan, An improved weighted recursive PCA algorithm for adaptive fault detection, Control Engineering Practice 50 (2016) 69–83.

[25] I. Markovsky, M. Niranjan, Approximate low-rank factorization with structured factors, Computational Statistics and Data Analysis 54 (2010) 3411–3420.

[26] Z. Fan, E. Liu, B. Xu, Weighted principal component analysis, in: Lecture Notes in Computer Science (including subseries Lecture Notes in Artificial Intelligence and Lecture Notes in Bioinformatics), pp. 569–574.

[27] A. Alkaya, I. Eker, Variance sensitive adaptive threshold-based PCA method for fault detection with experimental application, ISA Transactions 50 (2011) 287–302.

[28] S. Sels, S. Verspeek, B. Ribbens, B. Bogaerts, S. Vanlanduit, R. Penne, G. Steenackers, A cad matching method for 3d thermography of complex objects, 2019. Submitted for publication (Infrared Physics and Technology).